Computational Modeling for Cr and S Poisoning Pathways on $La_{0.6}Sr_{0.4}Co_{0.2}Fe_{0.8}O_3$ Surfaces

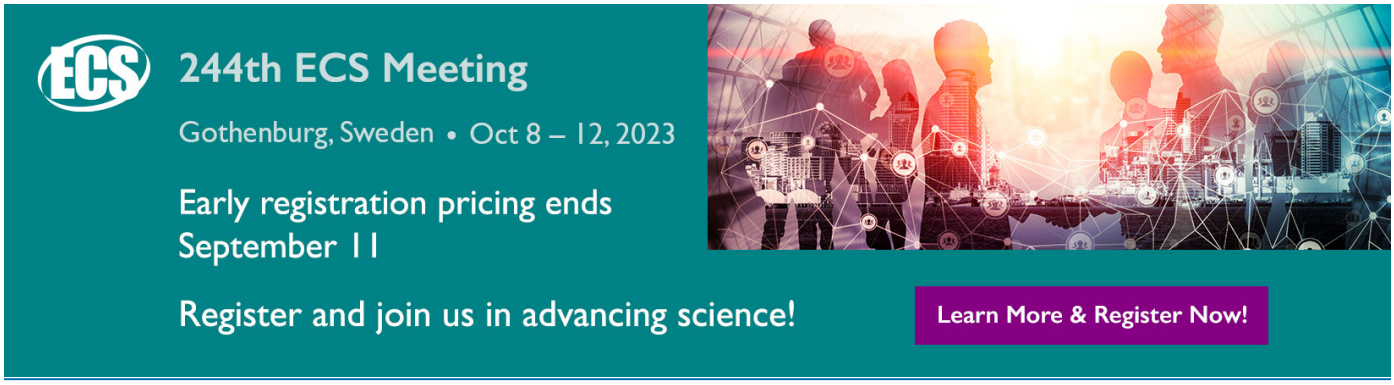

ECS Transactions, 111 (6) 743-751 (2023)
10.1149/11106.0743ecst ©The Electrochemical Society

Computational Modeling for Cr and S Poisoning Pathways on $La_{0.6}Sr_{0.4}Co_{0.2}Fe_{0.8}O_3$ Surfaces

B. Liu[a], and B. Yildiz[a,b]

[a] Department of Material Science and Engineering, Massachusetts Institute of Technology, Cambridge, Massachusetts 02139, USA
[b] Department of Nuclear Science and Engineering, Massachusetts Institute of Technology, Cambridge, Massachusetts 02139, USA

Solid oxide fuel cells (SOFCs) are highly efficient devices for energy conversion. However, their performance is hindered by the poisoning of their oxygen electrode materials by chromium and sulfur species. While previous studies have proposed a nucleation theory of Cr and S poisoning as a mechanism, little is known about the adsorption behaviors and compound formation steps during the poisoning process. This knowledge is critical for understanding the poisoning mechanisms and developing effective mitigation strategies. In this study, the state-of-the-art SOFC oxygen electrode material, $La_{0.6}Sr_{0.4}Co_{0.2}Fe_{0.8}O_3$ (LSCF), is used as a modeling system. A realistic surface structure will be constructed by grand canonical Monte Carlo (GCMC) simulation. Then, the adsorption energies as a function of surface chemistry will be calculated using density functional theory (DFT). The results revealed the importance of surface chemistry in determining the energetics and kinetics of precursor adsorption and compound formation.

Introduction

Solid oxide fuel cells (SOFCs) have the potential to play a significant role in various energy conversion applications, including power generation, transportation, and energy storage from renewable sources like wind and solar power (1–3). SOFCs' oxygen electrodes can act as catalysts in the electrochemical reduction of oxygen, resulting in the production of oxygen ions that can subsequently permeate through the electrolyte towards the anode (4). The performance of SOFCs depends on the efficiency of their oxygen electrode materials (5). Perovskite-based oxygen electrode materials, such as lanthanum strontium manganite (LSM), lanthanum strontium cobaltite (LSC), and lanthanum strontium cobalt ferrite (LSCF), have shown high efficiency and promise (6–8).

However, the performance and durability of perovskite-based oxygen electrode materials are limited by the degradation (9,10). This degradation is mainly caused by Sr segregation (11). This segregation may result in the formation of an insulating layer. With segregated surface Sr, the degraded electrode can be further poisoned by chromium (Cr) species from chromium-forming metallic interconnects and sulfur (S) species from fuels (12,13). These impurities significantly degrade the oxygen electrode performance by forming insulating surface layers or particles, such as $SrCrO_4$ and $SrSO_4$, and can reduce the performance and durability of SOFCs.

A nucleation theory has been proposed to understand the entire reaction in SOFCs (14,15). This theory proposes that the deposition of Cr and S onto SOFC oxygen electrode materials is through a process of nucleation and growth. Cr and S atoms react with the oxygen electrode surface to form small clusters or nuclei. These nuclei then grow and coalesce to form larger deposits of Cr and S on the surface. Using Cr as an example, the following equations depict nucleation reactions. Additionally, it has been observed that S species undergo analogous poisoning steps (16,17). The proposed generalized nucleation theory for CrO_3 postulates that the process initiates on the surface oxygen electrodes, which serve as surface active adsorption sites (e.g. surface Mn, Sr, Co, or Ba depend on materials), by means of the nucleation agent "*N*". This is then followed by Equations 1, 2, and 3.

$$N + CrO_3(g) \rightarrow Cr - N - O(nuclei) \quad (1)$$

$$Cr - N - O(nuclei) + CrO_3(g) \rightarrow Cr_2O_3(s) \quad (2)$$

$$Cr - N - O(nuclei) + N + CrO_3(g) \rightarrow N - Cr - O_{\times}(s) \quad (3)$$

Several experimental studies have observed the formation of Cr and S deposits on SOFC oxygen electrode surfaces and identified certain factors that can influence the nucleation and growth of Cr and S deposits, such as the fuel gas composition and operating temperature of the SOFCs (18–20) .

Surface Sr is one of the potential nucleation agents for Cr and S to deposit on (12,21). For LSCF, research has found that Sr ions generated by polarization and high temperatures could be the driving forces for the Cr and S poisoning. The pathways to Cr and S poisoning include the reaction of Cr and S with the segregated SrO at the surface. Insulating compounds such as $SrCrO_4$ and $SrSO_4$ are often found on the surface of oxygen electrodes containing Sr in the composition. Therefore, the surface segregated Sr^{2+} and SrO are strongly correlated with the poisoning processes.

Although there have been many experimental investigations, there is limited theoretical and computational modeling for Cr and S poisoning studies on SOFC oxygen electrode materials (12). Computational modeling is necessary for studying the poisoning in SOFC oxygen electrode materials because it provides insights into the specific reaction steps that are not easily obtainable through experimental investigations alone. However, previous computational studies have only focused on bulk materials' equilibrium thermodynamics and degradation modeling for a stack scale, neglecting the kinetics and reaction steps of the poisoning as a function of surface chemistry (20,22).

The pathways through which Cr and S poisoning occur have been relatively underexplored. Specifically, there is a lack of comprehension regarding the surface atomic structure of oxygen electrode at operational conditions. Without a realistic surface atomic structure, the Cr and S adsorption behaviors as a function of surface chemistry is less investigated. To address this gap in knowledge, this study uses LSCF as a model system. To accurately predict the LSCF surface atomic structures, both grand canonical Monte Carlo (GCMC) simulations and density functional theory (DFT) will be employed. Since simulating large systems like LSCF can be computationally expensive, acceleration methods like machine-learning trained interatomic potentials (IAPs) will also be utilized

(23). In order to comprehend the mechanisms and kinetics of Cr and S poisoning reactions, DFT will be employed to examine the deposition pathways of CrO_3 and SO_2, including adsorption with various configurations.

By acquiring a better understanding of the reaction pathways involved in Cr and S poisoning, we may be able to identify potential strategies for mitigating or preventing the negative effects of these poisons in SOFCs.

Method

GCMC simulation

The GCMC method is a physically motivated approach to explore the space of surface configurations (24–26). It enables the reconstruction process to move towards configurations that typically have lower surface energy. This method involves subjecting the surface to thermal (constant temperature) and chemical potential reservoirs (constant chemical potentials), which allow for fluctuations in the system's internal energies and the number of atoms. Figure 1 shows a typical workflow of the GCMC method. In each iteration, there are three possible actions: displacement of existing particles in the cell, insertion of new particles into the cell, and removal of particles from the cell. The probability of accepting an action of displace $P_{displace}$, an action of insert P_{insert}, and an action of remove P_{remove} are given by Equations 4, 5, and 6.

$$P_{displace} = min\left\{1, e^{-\frac{\Delta U}{k_B T}}\right\} \tag{4}$$

$$P_{insert} = min\left\{1, \frac{V}{(N+1)\Lambda^3} e^{-\frac{\Delta U - \mu}{k_B T}}\right\} \tag{5}$$

$$P_{remove} = min\left\{1, \frac{N\Lambda^3}{V} e^{-\frac{\Delta U + \mu}{k_B T}}\right\} \tag{6}$$

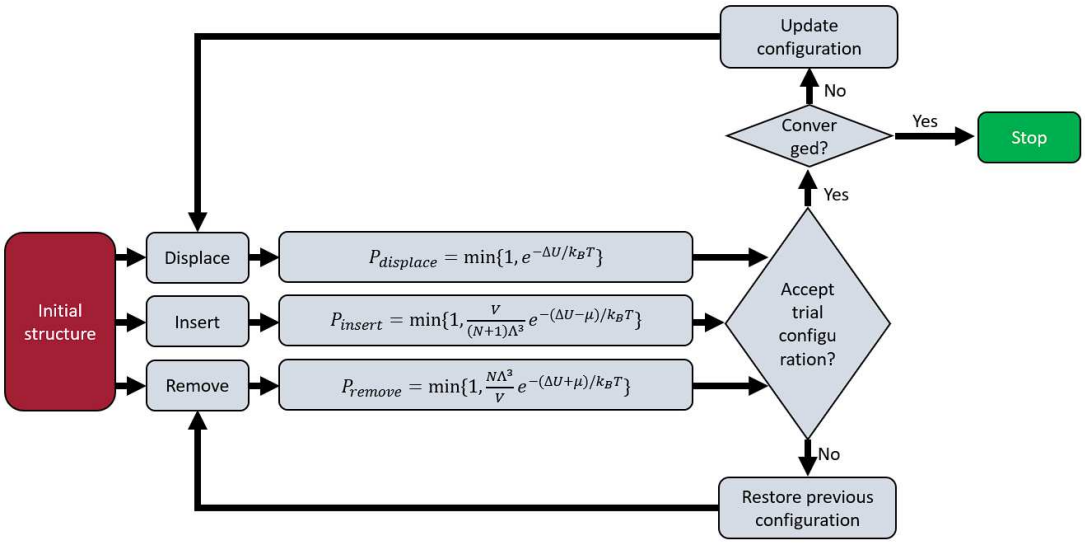

Figure 1. Flow diagram of GCMC method.

where N is the number of particles, V is the volume of the active GCMC in space, μ is the chemical potential of the atom that the action takes on, $\Lambda = \frac{h}{\sqrt{2\pi m k_B T}}$ is the thermal de Broglie wavelength, h is the Planck constant, m is the mass of the atom, and ΔU is the change in the internal energy. From Equations 1, 2, and 3, one can easily see that when the new structure reaches a lower internal energy state, the action is always accepted. If the action is accepted, a new action will be taken from the current structure. If the action is not accepted, the system will restore the previous structure to do another round of iteration.

Adsorption Energy Calculation

The adsorption energy calculations utilized the Vienna Ab initio Simulation Package (VASP) to perform DFT computations (27–30).The adsorption scheme is shown in Figure 2. The atoms' positions illustration was obtained using the VESTA software (31). The DFT electron wave functions and pseudopotentials are described using the projector augmented-wave (PAW) method, with the exchange and correlation (XC) potential implemented using the GGA-PBE functional revised for solids (PBEsol). To correct for self-interaction errors inherent in GGA functionals, the GGA + U method introduced by Dudarev et al. is used. The on-site correction is applied to the 3d manifolds of Fe^{3+} and Co^{3+}, with both a value of $U_{eff} = U - J = 4.0$ eV (32,33). The convergence criterion for electronic self-consistent field calculations (SCF) is set to 1×10^{-6} eV per atom, and the force convergence criterion for ionic relaxation is 3 mev per Å. The Kohn-Sham wave functions are expanded in plane waves up to an energy cutoff of 400 eV, with 0.05 eV of Gaussian smearing employed.

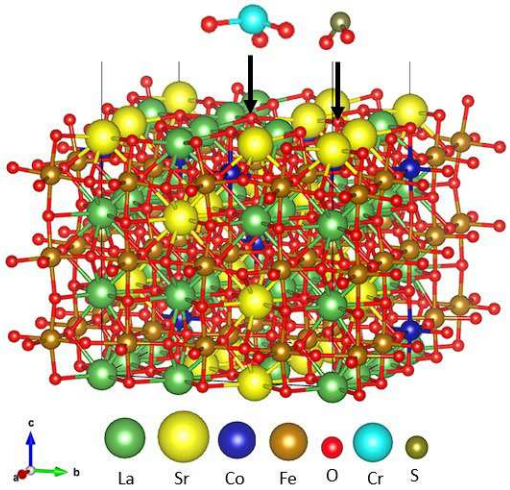

Figure 2. Schematics for adsorption. The atoms' positions illustrations are obtained using the VESTA software.

Both AO- and BO_2-terminated (001) LSCF slabs are constructed by two-dimensional 3 × 3 perovskite supercells in the xy-plane, with 7 or 8 layers in z-direction for AO- and BO_2-terminated slabs, respectively. The vacuum thickness of 20 Å is chosen to separate the two surface slabs to avoid artificial interactions between them. The lower 2 layers of slabs are set to be fixed in space, mimicking bulk LSCF structures and screening slabs from the bottom vacuum, whereas the upper layers are allowed to relax. A 3 × 3 × 1 Brillouin zone (BZ) sampling is performed using the Monkhorst–Pack grid (34). Several AO- and BO_2-terminated LSCF slabs will be constructed for the adsorption computation. To study

different adsorption configurations, for each slab, CrO_3 and SO_2 molecules will orient in parallel or perpendicular towards different surface oxygen or metal cations sites.

The adsorption energy E_{ads} can be calculated using Equation 7. The adsorption energy represents the difference in total energy between the relaxed slab with adsorbents and the energy of the pristine LSCF slab plus the total energy of an isolated CrO_3 or SO_2 molecule molecule.

$$E_{ads} = E_{system} - E_{slab} - E_{molecule} \tag{7}$$

where E_{system} is the total energy of the optimized slab with adsorbents, E_{slab} is the energy of the pristine LSCF slab and $E_{molecule}$ is the total energy of an isolated CrO_3 or SO_2 molecule. A larger negative E_{ads} value means a more stable configuration and exothermic adsorption.

Results and Discussion

GCMC simulation

To start GCMC simulations to find LSCF surface atomic structure, first need to identify the thermodynamic conditions that will be used. The temperature will be defined as 1073 K, as the commonly used temperature for current SOFC oxygen electrodes. The oxygen partial pressure is determined by the Equation 8, as a function of over potential based on the Nernst equation:

$$P_{O_2} = P_{O_{2,gas}} exp\left(-\eta \frac{4F}{RT}\right) \tag{8}$$

where $P_{O_{2,gas}}$ is the atmospheric oxygen partial pressure, η is the overpotential, F is Faraday's constant, R is the universal gas constant, and T is the absolute temperature. Using the overpotential relevant to application, 4 combinations of η ranging from 0 V to 0.51 V will be chosen, corresponding to $P_{O_{2,gas}}$ ranging from 0.2 atm to 10^{-10} atm. Table 1 summarizes all the conditions will be investigated.

TABLE I. Thermodynamic conditions will be applied for GCMC simulations.

Overpotential	Temperature	Effective partial pressure
0 V	1073 K	0.2 atm
0.18V	1073 K	10^{-4} atm
0.34 V	1073 K	10^{-7} atm
0.51 V	1073 K	10^{-10} atm

In Figure 3, a preliminary GCMC simulation was conducted at an effective oxygen partial pressure of 10^{-7} atm and a temperature of 1073 K. In Figure 3 a), the decreasing slab energies indicate that the GCMC algorithm is effectively driving the system towards a lower energy state. The starting structure, shown in Figure 3 b), is an AO-terminated surface composed of $La_{0.61}Sr_{0.39}Co_{0.14}Fe_{0.86}O_3$. Figure 3 c) displays the current most stable structure, which has a composition of $(La_{0.63}Sr_{0.37})_{1.36}Co_{0.22}Fe_{0.78}O_3$. This finding suggests that the surface composition can differ from the bulk composition, with deviations

observed in both the perovskite A-site and B-site composition and the stoichiometry. It is expected that the current most stable structure is A-site rich compared to B-site, as LSCF has been reported to have an A-site dominated termination on the surface region (35). Additionally, the upper surface layers of the current most stable structure are not in the perovskite phase as initially inputted, indicating a preference for a large surface reconstruction. This is consistent with experimental observations that multiple phases can coexist on the surface of LSCF, including Ruddlesden-Popper phase, SrO layers, or SrO particles (36,37).

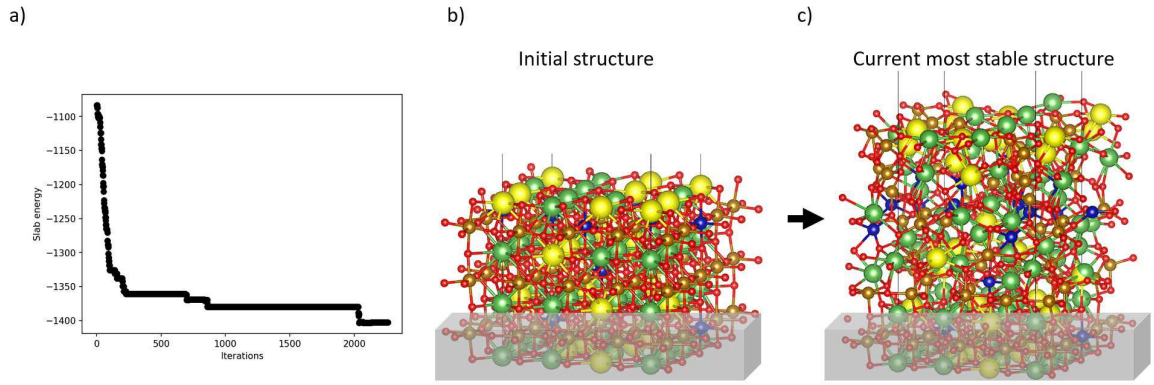

Figure 3. GCMC simulation of 1073 K and 10^{-7} atm effective oxygen partial pressure. a) Slab energies are decreasing as the GCMC iterations proceed. b) The starting slab structure at iteration = 0. c) The current most stable structure at iteration = 2000.

Adsorption Behaviors

To investigate the pathways of Cr and S poisoning, we plan to use realistic surface atomic structures of LSCF as reference states. However, due to the lengthy nature of GCMC simulations, we have first opted to examine the adsorption behaviors of Cr and S on LSCF surfaces terminated with perfect cleavage on the (001) planes. By gaining an understanding of how poisoning occurs on a perfectly cleaved (001) LSCF surface, we can then apply this knowledge to compare and contrast with reconstructed LSCF surfaces.

Multiple adsorption configurations, including different molecular orientations and slab compositions, will be investigated due to the vast adsorption configurational space where molecules can interact with LSCF surfaces. Several adsorption configurations will be considered on (001) LSCF surfaces, and their adsorption energies were found to vary. Figure 4 displays one of the most stable adsorption configurations for CrO_3 a) before and b) after adsorption on both AO- and BO_2-terminated slabs. Similar calculations were also performed to investigate the SO_2 adsorption behaviors. This specific adsorption configuration involves molecules attaching to the surface parallelly on the surface oxygen site, creating multiple bonds between surface oxygen anions and cations in molecules, and bonds between surface cations and oxygen anions in molecules. The corresponding adsorption energies are listed in Table 2.

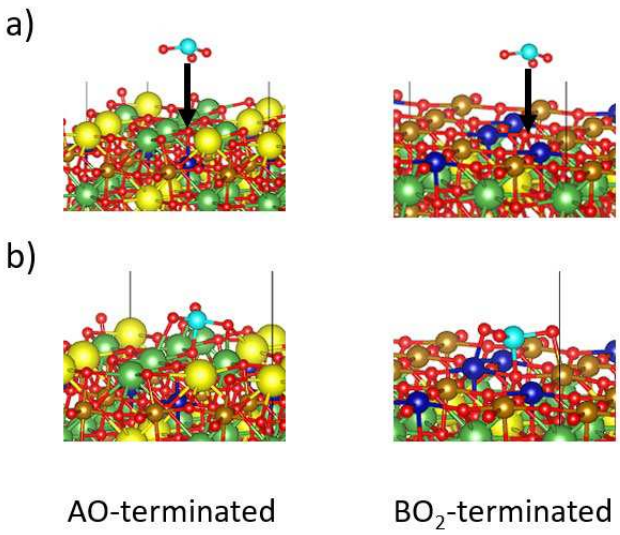

Figure 4. One of the most stable adsorption configurations for CrO_3 on (001) LSCF surfaces. a) before and b) after adsorption on both AO- and BO_2-terminated slabs

TABLE II The adsorption energies for the configurations shown in Figure 4.

Termination	E_{ads}
AO-termination	-5.3 eV
BO_2-termination	-3.0 eV

The surface oxygen site on LSCF slabs was found to be the most favorable site for the adsorption of CrO_3 and SO_2, as indicated by their highly negative adsorption energies. This suggests that the adsorption of these compounds is thermodynamically favorable, which has been previously observed experimentally but not confirmed through computational slab modeling (12,22). Moreover, the AO-terminated surface displayed more negative adsorption energies for CrO_3 and SO_2 than the BO_2-terminated surfaces. The calculated adsorption energy represents one configuration on each surface. In the future, the study will explore multiple configurations and extract trends as a function of surface chemistry and the chemistry and electronic structure of the adsorption site. This tendency will be characterized by surface-sensitive descriptors to gain a deeper understanding of the adsorption process. Additionally, molecular dynamics will be employed to investigate whether there is any tendency for the formation of compounds such as $SrCrO_4$ and $SrSO_4$ beyond mere adsorption.

Conclusion

This study uses computational simulations to identify the surface atomic structure and investigate the adsorption of Cr and S on LSCF surfaces. To achieve this, GCMC and DFT calculations were employed to determine surface configurations and locate the lowest energy surface structures under different thermodynamic conditions. DFT was also used to calculate the energetics of adsorption as a function of configuration. The findings showed that the surface chemistry plays a crucial role in determining the reaction pathways. Specifically, the GCMC algorithm was found to effectively drive the system towards a lower energy state, resulting in composition deviations in both the perovskite A-site and B-site composition and the stoichiometry. The study also found that the adsorption of both

molecules on the LSCF surface was thermodynamically favorable, and identified the most stable adsorption configuration where the molecules adsorb on the LSCF surface parallel via surface oxygen anions on the AO-termination. Overall, these results provide valuable insights into the mechanisms of SOFC electrode poisoning and pave the way for further computational and experimental investigations in this field.

Acknowledgments

This study is supported by the U.S. Department of Energy - NETL DE-FE0032102. The author wants to acknowledge Texas Advanced Computing Center (TACC) and MIT Engaging for providing computational resources. The author expresses gratitude to Filip Grajkowski and Sophie Coppieters 't Wallant for providing important experimental insights.

References

1. A. Hauch, R. Küngas, P. Blennow, A.B. Hansen, J.B. Hansen, B. V. Mathiesen, M.B. Mogensen, *Science (1979)*, 370 (2020).
2. K.T. Lee, E.D. Wachsman, *MRS Bull*, 39 (2014) 783–791.
3. D. Neagu, G. Tsekouras, D.N. Miller, H. Ménard, J.T.S. Irvine, *Nat Chem*, 5 (2013) 916–923.
4. S. Elangovan, J.J. Hartvigsen, L.J. Frost, *Int J Appl Ceram Technol*, 4 (2007) 109–118.
5. A. Hauch, S.H. Jensen, S. Ramousse, M. Mogensen, *J Electrochem Soc*, 153 (2006) A1741.
6. L.Y. Woo, R.S. Glass, R.J. Gorte, C.A. Orme, A.J. Nelson, *J Electrochem Soc*, 156 (2009) B602.
7. G.M. Rupp, A. Limbeck, M. Kubicek, A. Penn, M. Stöger-Pollach, G. Friedbacher, J. Fleig, *J. Mater. Chem. A*, 2 (2014) 7099–7108.
8. M. Liu, D. Ding, K. Blinn, X. Li, L. Nie, M. Liu, *Int J Hydrogen Energy*, 37 (2012) 8613–8620.
9. C. Graves, S.D. Ebbesen, S.H. Jensen, S.B. Simonsen, M.B. Mogensen, *Nat Mater*, 14 (2015) 239–244.
10. A. Hauch, S.H. Jensen, S. Ramousse, M. Mogensen, *J Electrochem Soc*, 153 (2006) A1741.
11. K. Chen, S.P. Jiang, *Electrochemical Energy Reviews*, 3 (2020) 730–765.
12. L. Zhou, J.H. Mason, W. Li, X. Liu, *Renewable and Sustainable Energy Reviews*, 134 (2020).
13. S. Krishnan, M.K. Mahapatra, P. Singh, R. Ramprasad, *Comput Mater Sci*, 137 (2017) 6–9.
14. L. Zhao, J. Drennan, C. Kong, S. Amarasinghe, S.P. Jiang, *J Mater Chem A Mater*, 2 (2014) 11114–11123.
15. S.P. Jiang, J.P. Zhang, L. Apateanu, K. Foger, Deposition of Chromium Species at Sr-Doped LaMnO 3 Electrodes in Solid Oxide Fuel Cells. I. Mechanism and Kinetics, (2000).
16. F. Wang, H. Kishimoto, T. Ishiyama, K. Develos-Bagarinao, K. Yamaji, T. Horita, H. Yokokawa, *J Power Sources*, 478 (2020).

17. C. Riedl, M. Siebenhofer, A. Nenning, A. Schmid, M. Weiss, C. Rameshan, A. Limbeck, M. Kubicek, A.K. Opitz, J. Fleig, *J Mater Chem A Mater*, 10 (2022) 14838–14848.
18. C.C. Wang, M. Gholizadeh, B. Hou, X. Fan, *RSC Adv*, 11 (2021) 7–14.
19. N. Schrödl, A. Egger, J. Lammer, F. Hofer, W. Sitte, *J Electrochem Soc*, 168 (2021) 014509.
20. R. Sachitanand, M. Sattari, J.E. Svensson, J. Froitzheim, *Int J Hydrogen Energy*, 38 (2013) 15328–15334.
21. X. Yin, L. Bencze, V. Motalov, R. Spatschek, L. Singheiser, *Int J Appl Ceram Technol*, 15 (2018) 380–390.
22. S. Krishnan, M.K. Mahapatra, P. Singh, R. Ramprasad, *Comput Mater Sci*, 137 (2017) 6–9.
23. C. Chen, S.P. Ong, *Nat Comput Sci*, 2 (2022) 718–728.
24. T.P. Senftle, R.J. Meyer, M.J. Janik, A.C.T. van Duin, *J Chem Phys*, 139 (2013) 044109.
25. T.P. Senftle, A.C.T. van Duin, M.J. Janik, *Catal Commun*, 52 (2014) 72–77.
26. V. Somjit, B. Yildiz, *ACS Appl Mater Interfaces*, 14 (2022) 42613–42627.
27. G. Kresse, J. Furthmüller, *Comput Mater Sci*, 6 (1996) 15–50.
28. G. Kresse, Ab Initio Molecular-Dynamics Simulation of the Liquid-Metal-Amorphous-Semiconductor Transition in Germanium, (n.d.).
29. G. Kresse, J. Hafner, Ab. Initio Molecular Dynamics for Liquid Metals, (n.d.).
30. G. Kresse, J. Furthmü, Efficient Iterative Schemes for Ab Initio Total-Energy Calculations Using a Plane-Wave Basis Set, (1996).
31. K. Momma, F. Izumi, *J Appl Crystallogr*, 44 (2011) 1272–1276.
32. A.M. Ritzmann, J.M. Dieterich, E.A. Carter, *Physical Chemistry Chemical Physics*, 18 (2016) 12260–12269.
33. L. Ma, P. Priya, N.R. Aluru, *J Electrochem Soc*, 165 (2018) F1232–F1241.
34. P. Wisesa, K.A. McGill, T. Mueller, *Phys Rev B*, 93 (2016) 155109.
35. J. Druce, H. Téllez, M. Burriel, M.D. Sharp, L.J. Fawcett, S.N. Cook, D.S. McPhail, T. Ishihara, H.H. Brongersma, J.A. Kilner, *Energy Environ. Sci.*, 7 (2014) 3593–3599.
36. D. Oh, D. Gostovic, E.D. Wachsman, *J Mater Res*, 27 (2012) 1992–1999.
37. S. He, M. Saunders, K. Chen, H. Gao, A. Suvorova, W.D.A. Rickard, Z. Quadir, C.Q. Cui, S.P. Jiang, *J Electrochem Soc*, 165 (2018) F417–F429.